Organic-Inorganic halide perovskites: an ambipolar class of materials with enhanced photovoltaic performances

Giacomo Giorgi and Koichi Yamashita[1]

[1]Department of Chemical System Engineering, School of Engineering, The University of Tokyo, 7-3-1, Hongo, Bunkyo-ku, Tokyo, Japan & CREST-JST, 7 Gobancho, Chiyoda-ku, Tokyo 102-0076, Japan.

Email: giacomo@tcl.t.u-tokyo.ac.jp ; yamasita@chemsys.t.u-tokyo.ac.jp

Abstract

After a brief introduction concerning the general properties of the perovskite class of materials, we review the most relevant contributions to studies on organic–inorganic halide perovskites concerning their application as photovoltaics. Moving on from the rise of a new solar cell assembly procedure (Kojima *et al.*, *J. Am. Chem. Soc.*, 2009, **131**, 6050–6051), we focus on the main developments that have occurred over the last five years that have led to high photoconversion efficiencies. We particularly refer to the contribution provided by theoreticians, and how a synergy between theoreticians and experimentalists has enabled us to understand many fundamental characteristics of such an extremely appealing class of materials. Particular attention is devoted towards the *ambipolar* (i.e., both *p*- and *n*-conductive) nature of organic–inorganic halide perovskites, and to the role that the methylammonium cation plays in the structural and electronic properties of these compounds.

1. Perovskite, the philosopher's stone of materials science

Having been discovered by Gustav Rose in 1839, perovskites, whose prototypical mineral has the chemical formula $CaTiO_3$, represent a class of materials with unique features that are nowadays revealing their manifold and versatile applicability in a large range of technological devices. They have the general chemical formula ABX_3, where the "A" ion (represented by (0.0; 0.0; 0.0) in the crystal coordinates of an ideal cubic structure) and the "B" ion (represented by (0.5; 0.5; 0.5)) are both cations with usually noticeably different radii and "X" is an anion site (in each of the face centered

positions, (0.5, 0.5, 0.0)). Their stability is determined by the Goldschmidt tolerance factor "t" [1], which in the case of X being an oxygen anion is given by

$$t = (R_A + R_O) / \sqrt{2} (R_B + R_O), \qquad (1)$$

where R_A, R_B, and R_O represent the ionic radii of the A and B cations and the oxygen anion, respectively. The ideal cubic structure ($t = 1$) is not very common: at room temperature [2] $SrTiO_3$ represents one of the very few ideal cubic perovskite structures [3]. The cubic structure usually occurs in the range $0.89 < t < 1$ [3–5], as when $t > 1$ hexagonal structures prevail (i.e., $BaNiO_3$ type), while for $t < 0.89$, orthorhombic structures are predicted, as in the case of $GdFeO_3$ ($t = 0.81$) [3].

The tolerance factor has been widely used over the years as a criterion for discussing the stability of several perovskites containing other anions, i.e., chlorides [6] and fluorides [7], and has even been extended to the case of ABO_3 crystals with the ilmenite structure ($t < 0.8$) [8]. The conventional ABX_3 cubic structure is shown in Fig. 1.
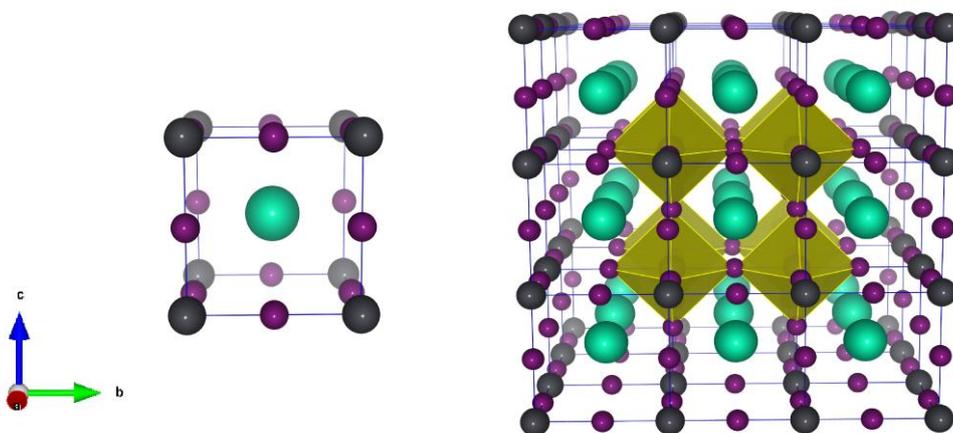
Fig. 1: The highly symmetrical cubic perovskite structure. Key: green = A cation site, gray = B cation site, and purple = X anion site. Left-hand side = unit cell and right-hand side = supercell.

The strict constraint given by the tolerance factor makes other noncubic polymorphs common. Similarly, the strong relationship between the tilt angles of the perovskite octahedra and the final geometry of the unit cell is responsible for the possible,

reversible, phase transitions that occur between all the accessible polymorphs (cubic, tetragonal, orthorhombic, and monoclinic) [2, 9].

Piezoelectricity [10], pyroelectricity [11, 12], colossal magnetoresistivity [12], high-temperature superconductivity [13], and electro-optic effects [14] are just a few of the properties characterizing perovskites. Although the oxide class represents the most abundant and investigated class of materials, halides, sulfides, nitrides, hydrides, oxyhalides, and oxynitrides are similarly known experimentally and have been characterized. Among these classes, a special mention is deserved by the oxynitrides, a class of perovskites recently studied for their high potential in optics and photocatalysis [15].

An emerging class in photovoltaics (PV) is represented by the halide perovskites, both as fully inorganic materials and as hybrid organic–inorganic materials (ABX_3, where A = an alkali/organic cation, B = Ge, Sn, or Pb, and X = halide ion). In such compounds, the total valence of the two cations must be equal to three, with the only possible combination being $A^I–B^{II}–X_3$. In the case of the hybrid organic–inorganic halide perovskites, the monovalent inorganic cation is replaced by a molecular organic cation (with methylammonium (MA, $CH_3NH_3^+$), formamidinium (FA, $H_2N–CH=NH_2^+$), and tetramethylammonium (TMA, $(CH_3)_4N^+$) being among the most common encountered). The ionic radius of the organic cation has an influence on the stability of the final structure: larger cations lead to the dissolution of the three-dimensional (3D) structure and make the crystals assume structures with a lower dimensionality. Noticeably, such two-dimensional (2D) crystals have already been the subject of intense interest during the 1990s for utilization in optoelectronics, as witnessed by the relevance of this class of materials in technologically oriented applications [16–21].

The initial tolerance factor formula of Goldschmidt has been extended to include these novel materials [22] by taking into account the fact that the presence of molecular organic cations means that they are able to interact via hydrogen bonds within a semiconductor network, and this makes the calculation of their molecular ionic radii a challenging task. Moving on from the initial work of Mitzi, who applied the Goldschmidt tolerance factor to the case of lead iodide organic–inorganic perovskites [23], Kieslich [22] reformulated the initial equation of Goldschmidt and introduced a term known as the effective ionic radius, R_{Aeff}, applying it to both iodides ($X = I^-$) and formates ($X = HCOO^-$):

$$R_{Aeff} = R_{mass} + R_{ion} \qquad (2).$$

The effective ionic radius, R_{Aeff}, results from the sum of two contributions: the distance between the center of mass of a molecule and the atom with the longest distance to the center of mass (R_{mass}) and the corresponding ionic radius of such an atom (R_{ion} [2]). Despite an uncertainty in the tolerance factor of ~6%, this formulation allows us to better take into account the molecular nature of the cations [22].

2. Organic–inorganic halide perovskites: from optoelectronics to photovoltaics

2.1 The experimental scenario

In the longstanding research of novel performing materials for photovoltaic applications, recently enhanced photoconversion efficiencies (PCEs) up to more than 15% [24-26] (Sang Il Seok group at KRICT reached certified PCE of 17.9%) have been reported in literature for organic-inorganic solar cells containing mixed organic-inorganic perovskite halides, as novel light harvester, assembled with an inorganic supporting material, mesoporous TiO_2 [27-29], and a polymeric hole transporting material (HTM).

Despite the fact that impressively high PCEs have been already achieved with such a novel device architecture that is still in its infancy, many of the structural, electronic, and optical properties remain to be fully elucidated, revealing the enormous potential for such materials in PV applications. To highlight the progress in organic–inorganic perovskites in solar devices, the first review and commentary papers have recently appeared in the literature describing the state of the art of this new architecture device technology [30–38].

Tridimensional $MAPbX_3$ (plumbates) [39, 40] and $MASnX_3$ (stannates) compounds [41, 42] are characterized by having a high chemical stability and good transport characteristics once they are in contact with the mesoporous oxide layer used in assembling solar devices. $MAPbX_3$, obtained by replacing Cs cations with MA cations, is a relatively recent synthetic achievement (1978) [43] compared with $CsPbX_3$ halide perovskites, which are a well-known and characterized class of materials known for over a century. A proper knowledge of $MAPbX_3$ polymorphism [39, 43, 44] is one of the key steps towards obtaining a full understanding of their role in perovskite-based solar devices. Mixed organic–inorganic halide perovskites do

indeed exist in different phases: Poglitsch and Weber have reported the cubic phase (*Pm3m*) [39] as being the most stable phase at ambient temperature for the lighter halides, i.e., $MAPbCl_3$ and $MAPbBr_3$, while in the case of the iodide compounds, the same cubic polymorph becomes stable at $T_c > 327.4$ K, with the tetragonal phase (*I4/mcm*) being the most stable phase under ordinary conditions [44].

Full characterization of AMI_3 compounds (A = MA, FA, and M = Sn, Pb) and also of the $MASn_{1-x}Pb_xI_3$ has been carried out by Stoumpos *et al.* [45]. Their experiments have shown that this class of compound can act as both *n*-type and *p*-type semiconductors, depending on the synthesis methodology used, with the former compounds obtained from solution and characterized by having the lowest carrier concentration and the latter compounds being synthesized using solid state reactions. These materials are characterized by having extremely high carrier mobilities (2000 $cm^2/(Vs)$ and 300 $cm^2/(Vs)$ for electrons and holes, respectively) [45]. Using several techniques (PL, FT-IR, Seebeck coefficient, and Hall effect measurements), all the possible phase transitions occurring in these crystals have been reported. Similarly, an overall marked tendency for the Sn compounds to undergo oxidation was detected, with the *p*-type Sn^{4+}-doped semiconductors exhibiting metallic conductivity [45]. This finding provides clear evidence that Pb halide perovskites are better materials for PV applications.

The recent story of organic–inorganic perovskites as light harvesters in solar cells began with the pioneering work of Miyasaka *et al.* [46], where the initial Br and I cells achieved PCE values of 3.8% and 3.1%, respectively. These prototypical devices were assembled according to the conventional dye-sensitized solar cell (DSSC) architecture employing a liquid electrolyte.

Similarly, use of a liquid electrolyte also characterized the cells fabricated by Im *et al.* [47], where a PCE of about 6.5% was achieved for perovskite quantum dot-sensitized cells fabricated using a spin-coating technique employing MAI and PbI_2 as precursors. The photocurrent density (J_{sc}) of such devices reached much higher values compared with those using standard N719-sensitized devices. Nevertheless, the physiological degradation of cells with liquid electrolytes had a detrimental effect on the final performance of the device, and this has motivated the replacement of liquid electrolytes with a solid HTM. Accordingly, as a further evolution of the initial cells of Miyasaka, 2,2′,7,7′-tetrakis (N,N-di-p-methoxyphenylamine)-9,9′-spirobifluorene

(Spiro-OMeTAD) has been introduced as an HTM, and has led to a marked improvement in the stability of the final device. In particular, in the cell fabricated by Kim *et al.* [29], analysis using a femtosecond laser in conjunction with photoinduced absorption measurements indicated that a two-step charge separation process occurred, consisting of a hole-injection step from the excited nanoparticles into the Spiro-OMeTAD molecules followed by an electron-transfer step to the mesoscopic TiO_2 film. A PCE of 9.7% was reported for this device.

The impact of the HTM on the performance of solar devices has also been the topic of active analysis [48]: the photovoltaic properties of $HTM/MAPbI_3/TiO_2$ solar cells using Spiro-OMeTAD, poly(3-hexylthiophene-2,5-diyl) (P3HT), and 4-(diethylamino)-benzaldehyde diphenylhydrazone (DEH) as the HTM were tested and compared. The best performance was obtained using Spiro-OMeTAD (PCE = 8.5%) under an AM 1.5G illumination with a power density of 1000 W/m^2. Moreover, despite the similar charge-transport properties between these three HTMs, electron lifetime measurements showed that the charge recombination in cells using DEH was ten times faster than for P3HT, and was one hundred times faster than for Spiro-OMeTAD, thus suggesting that the reason for the different performances of these HTMs was the different electron lifetimes.

Despite the enhanced performance from the use of Spiro-OMeTAD, employing this compound is accompanied by several drawbacks. The main drawback is related to the high series resistance encountered, which reduces the fill factor and subsequently worsens the final PCE value of the cell. One way to overcome such a drawback is to enhance the poor charge-transport properties of Spiro-OMeTAD using *p*-doping. In particular, Noh *et al.* [49] obtained a PCE of 10.4% using Spiro-OMeTAD doped with tris (2-(1*H*-pyrazol-1-yl)-4-*tert*-butylpyridine) cobalt(III) tris (bis (trifluoromethylsulfonyl) imide)) (FK209). There is clear evidence that the use of both doped and nondoped Spiro-OMeTAD can be avoided by taking advantage of the *ambipolar* nature of hybrid organic–inorganic perovskites (being both *p*- and *n*-conductor materials, in addition to their light harvester role). In this context, Etgar *et al.* [50, 51] showed that $MAPbI_3$ could play an efficient role not only as a light harvester (*vide supra*) but also as an HTM. This striking property enables us to assemble cells containing $MAPbI_3/TiO_2$ heterojunctions, which have a PCE of 7.3%. The scheme used in Etgar's device is shown in Fig. 2, along with the energy level diagram for the heterojunction cell.

Alternatively, using an extremely thin absorber (ETA) approach and employing Spiro-OMeTAD as an HTM, Lee *et al.* [52] have reported low-cost solution-processable stable solar cells with insulating Al_2O_3 replacing the mesoporous TiO_2 layer. These cells had an improved PCE of 10.9% (*c.f.* 8% using mesoporous TiO_2). In these so-called mesosuperstructured solar cells (MSSCs), alumina acts as an inert scaffold that keeps electrons within the perovskite layer, making them flow through the perovskite itself.
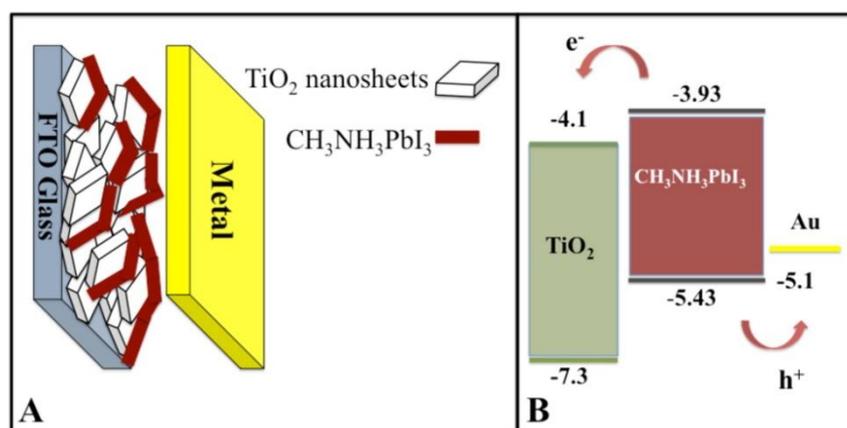

Fig. 2: (a) Scheme of Etgar's device structure. (b) Energy level diagram of a $CH_3NH_3PbI_3/TiO_2$ heterojunction solar cell. (Reprinted with permission from Ref. [50]. Copyright 2012 American Chemical Society.)

The perovskite used in these cells was the mixed perovskite $MAPbI_2Cl$ (or Cl-doped $MAPbI_3$ [37]). The use of this material led to an impressive reduction in the fundamental losses, with the most efficient device exhibiting a short-circuit photocurrent of 17.8 mAcm^{-2}, a V_{oc} of 0.98 V, and a fill factor of 0.63. The enhanced V_{oc} value in these devices is associated with the confinement of the electrons in the perovskite layer, which increases the splitting of the quasi-Fermi levels for the carriers under illumination. The working principle of the two devices (i.e., the perovskite-sensitized TiO_2 and the noninjecting Al_2O_3-based devices) is shown in Fig. 3. Here, it can be seen that the band gap of Al_2O_3 is too wide to allow electrons to pass from the perovskite Conduction Band Maximum (CBM) to the Al_2O_3 band, confining the photoexcited electrons within the perovskite region.
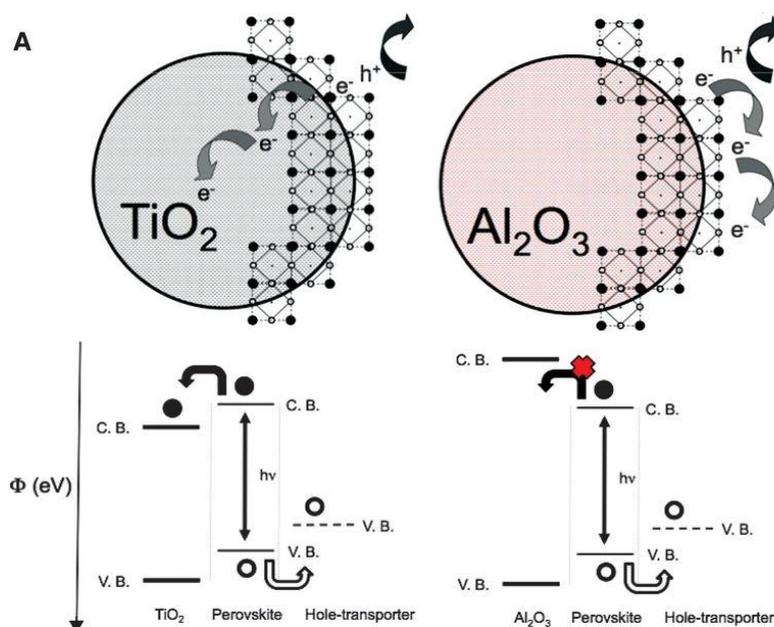
Fig. 3: A schematic drawing showing charge transfer and charge transport in a perovskite-sensitized TiO_2 solar cell (left-hand side) and a noninjecting Al_2O_3-based solar cell (right-hand side). A representation of the energy landscape is shown below, with the electrons shown as solid circles and the holes shown as open circles. (From Ref. [52]. Reprinted with permission from AAAS.)

Similar to the case of the cells used by Etgar [50], where the dual nature of light absorber and HTM was reported for $MAPbI_3$, the cells fabricated by Lee [52] also operated by taking advantage of the dual nature of these perovskites. In this case, the perovskite compound played the role of light harvester and electron transport material. More recently, Snaith introduced a very appealing alternative architecture to the mesoporous perovskite-sensitized oxide perovskite-containing devices. Snaith's assembly procedure took into account the possibility of using a simple planar heterojunction thin-film solar cell [25] incorporating a vapor-deposited perovskite $MAPbI_{3-x}Cl_x$ absorber and achieved efficiencies > 15%. This p-i-n device architecture exploited the reported long carrier lifetimes of these perovskite materials, for which the electron–hole diffusion lengths are > 100 nm for pure $MAPbI_3$ and 1 μm for Cl-doped $MAPbI_3$ [53, 54]. The organic and inorganic precursors used in these cells were methylammonium iodide (MAI) and lead chloride ($PbCl_2$), respectively. The most efficient vapor-deposited (or solution-processed) planar heterojunction was characterized as having a J_{sc} of 21.5 $mAcm^{-2}$ (17.6 $mAcm^{-2}$), a V_{oc} of 1.07 V (0.84 V), and a fill factor of 0.68 (0.58), with an overall PCE of 15.4% (8.6%). These high PCE

values show that a nanostructuring procedure is not mandatory to assemble perovskite solar devices. A scheme showing both the vapor-deposited and solution-processed cells is presented in Fig. 4.
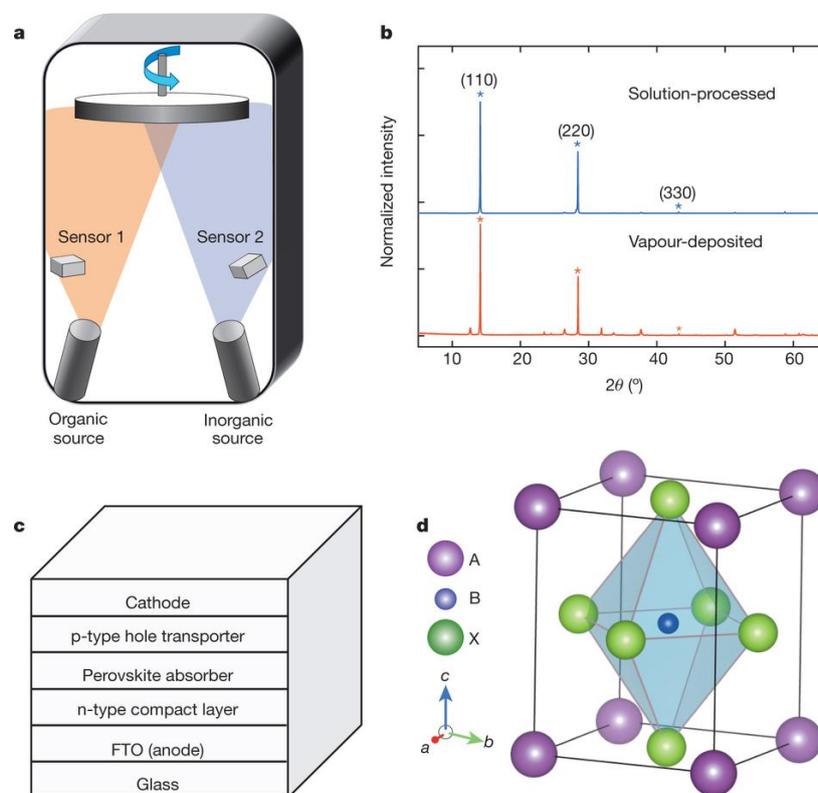

Fig. 4: (a) A dual-source thermal evaporation system for depositing perovskite absorbers. The organic source used was methylammonium iodide and the inorganic source used was $PbCl_2$. (b) X-ray diffraction spectra of a solution-processed perovskite film (blue) and a vapor-deposited perovskite film (red). The baseline is offset for ease of comparison and the peak intensity has been normalized. (c) A generic structure of a planar heterojunction p–i–n perovskite solar cell. (d) Crystal structure of a perovskite absorber adopting the perovskite ABX_3 form, where A is methylammonium, B is Pb, and X is either I or Cl. (Reprinted with permission from Macmillan Publishers Ltd: Nature, Ref. [25], copyright (2013).)

The introduction of low-temperature (low-T)-processed solar devices (T < 150 °C) was the fundamental breakthrough of Snaith's group. Low-T-processed absorbers not only still fulfill the main operations in solar cells, but also greatly simplify the architecture of the device. Moreover, high-temperature (high-T) sintering of the

scaffold layer (Al_2O_3) serves no electronic purpose [55]. In the case of compact layers of titania [26], high-T processing is even more detrimental because it is considered to be responsible for the series resistance observed in solar cells. Using low-T-processed compact titania layers, a PCE of 15.9% has been achieved because of the higher fill factor that was achieved (and is consistent with the observed decrease in the series resistance).

More recently, a planar device configuration similar to that of Al_2O_3 MSSCs showed severe hysteresis effects in the current–voltage curves in the slow-scan-rate regime [56]. Several possible reasons were cited to explain this behavior: (1) the high defect density within or near to the surface, (2) the similarity to the ferroelectric nature of perovskites (slow polarization of the material on applying a bias), and (3) an excess of interstitial defects (from iodide or MA ions), which were supposed to be the cause of the hysteresis of the curves. Investigations into understanding such anomalous behavior are currently in progress.

A recent interesting technique for fabricating perovskite thin films, and thus PV films, with planar geometry is the low-temperature (T < 150 °C) vapor-assisted-solution process (VASP) [57], whose crucial step involves film growth via an *in situ* reaction of an as-deposited film of PbI_2 with MAI vapor. This technique takes advantage of two of the properties of the materials involved: the kinetic reactivity of MAI and the thermodynamic stability of the resulting perovskite (factors that lead to full surface coverage and reduced superficial roughness). The efficiencies obtained using this technique exceed 12%.

2.2 The theoretical scenario

Parallel to the efforts of the experimentalists, theoreticians have greatly improved the basic knowledge of structural, electronic, and optical properties of hybrid organic–inorganic perovskites. In this context, density functional theory (DFT) and post-DFT methods have been widely employed to model experimental results, and similar to the predictive tools, have suggested viable improvements in the properties of perovskite-based solar devices.

The analysis and knowledge of the intrinsic defect behavior of semiconductors represented the first step towards their optimized use in technological applications. A well-researched case involving $MAPbI_3$ identified unintentional doping and its

possible coexistence with a long carrier diffusion length typical of such perovskites [58]. Starting from the orthorhombic structure of $MAPbI_3$ ($a = 9.25$, $b = 12.89$, $c = 8.63$ Å, DFT/GGA level), Kim *et al.* investigated the formation of both Schottky (PbI_2 and MAI vacancies) and Frenkel (Pb, I, and MA vacancies) defects. Neither MAI nor PbI_2 have any trapping states in their band gaps. Frenkel-derived defects form in shallow levels near the band edges, and are considered to be sources of unintentional doping. This result clearly explains why the presence of such defects does not impact on the diffusion length and the carrier lifetime. Moreover [59], low formation energy defects induce only shallow levels while, at variance, defects with deep levels in the gap require high energies to be formed . Frenkel defects (Pb vacancies) are the most abundant under *p*-type conditions (associated with the destabilizing Pb 6s–I 5p antibonding orbital overlap, which facilitates the formation of Pb vacancies), while interstitial MA defects are dominant under *n*-type conditions (associated with weak semiconductor–barrier [40] Van der Waals interactions), confirming at the theoretical level the experimentally reported dependence of the electronic properties of $MAPbI_3$ on the growth conditions.

The calculations of Du reveal that among native point defects [60], only iodine vacancies are low-energy deep traps and non-radiative recombination centers. The formation of the iodide–chloride mixed alloy decreases the lattice constant of the iodine site, inducing an increase in the formation energy of the interstitial defects, providing theoretical evidence of the observed increase in carrier diffusion length in Cl-doped $MAPbI_3$ with respect to the pure crystal.

Interestingly, there is a strong relationship between the electronic properties of the surface and those of the defects in the bulk: the absence of states in the gap for a flat and a vacant termination on the most stable (110) and (001) surfaces of $MAPbI_3$ clearly reveals the contribution of such surfaces to the experimentally reported long carrier lifetimes of perovskite solar cells [61].

Among the theoretical groups involved in the study of such novel hybrid materials, De Angelis's group surely represents one of the most active [62–69]. Using a DFT approach [62], De Angelis's group has characterized the electronic properties of the 3D mixed halide $MAPbI_2X$ perovskites (X = Cl, Br, I). Here, two different stable structures (1) head-to-head (referring to the orientation of the organic moiety inside the semiconductor network) and (2) head-to-tail exist (as shown in Fig. 5), with their stability depending on the nature of the halide ion, X.
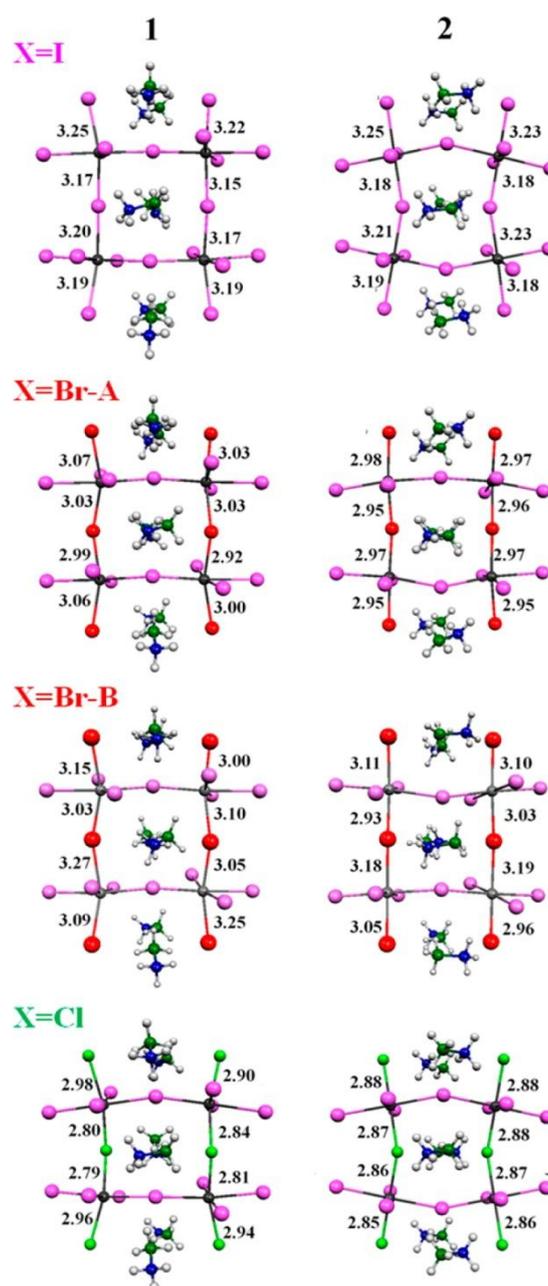
Fig. 5: Optimized geometrical structures of Type 1 (left-hand side) and Type 2 (right-hand side) MAPbI$_2$X, along with the main geometrical parameters. Key: X = I, purple; X = Br, red; X = Cl, green. The structures obtained using the A and B lattice parameters are reported for MAPbI$_2$Br. (Reprinted with permission from Ref. [62]. Copyright 2013 American Chemical Society.)

The same electronic band gap was predicted for the two structures in the case of X = I, while the Br and Cl systems had a sizeable difference in their band gaps. For the X = I case, the most stable structure was characterized by a head-to-tail orientation of the

organic cations in a fashion that closely resembles the orthorhombic polymorph. The Br–I mixed perovskite has a wider band gap than the pure I compound, while similar band gaps characterize the Cl–I mixed compound and MAPbI$_3$. In terms of stability, the mixed Br–I compound is characterized by having a formation energy intermediate between the iodide and the mixed Cl–I compounds. This analysis had the clear goal of shedding light on the onset of optical absorption of possible perovskite absorbers, since the J_{sc} value of the final device is strongly influenced by these characteristics of the materials.

The same group of De Angelis, in a combined theoretical/experimental study [63], examined the role that chloride ions play as a dopant on the transport properties of these materials. The addition of Cl ions into MAPbI$_3$ at relatively low concentrations (up to 4%) does not have a significant influence on the band gap of the material, but it does improve the charge-transport properties of the perovskite, further supporting the experimentally reported improved performance of mixed halide MSSC devices [52]. Another very active group in this field is led by Even [70–74], and has provided a sound explanation for the improved transport properties induced by doping in terms of collective molecular motion hindering [70]. The collective molecular motion of the organic cations observed at room temperature is considered to be responsible for the exciton screening associated with the free carriers in these materials [55, 75]. Consistent with the larger carrier mobility induced by doping, Even *et al.* [70] found that the inclusion of a halide atom having a different ionic radius in mixed perovskites is highly beneficial in avoiding such collective motion that otherwise is responsible for the decreased optical absorption.

As mentioned previously, hysteresis in thin-layer heterojunctions represents one of the most serious and detrimental drawbacks of their assembly procedures [56], and one of the possible origins of such behavior is ascribed to the ferroelectric properties of perovskites conferring a possible slow polarization of the material on applying a bias [45]. Frost *et al.* [76] showed that these perovskites exhibit spontaneous electric polarization, with a low barrier for rotation of the organic cations and the absence of long-range ordering of the molecular dipoles of the MA cations. The presence of an external electric field can radically change such behavior, and in the presence of light (as in PV devices) a transition from paraelectric to ferroelectric ordering would enhance the electron–hole separation distance.

Gottesmann *et al.* [69] combined experimental and DFT-based results and suggested a possible interpretation for the mechanism of hysteresis. MA cations were predicted to rotate and align along the electric field, altering the structure of the lead–iodine network. Such a process seems to take place on a different time scale (fast cation alignment and slow inorganic alignment). This is reflected in the very slow photoconductivity response, and provides a plausible explanation of the experimentally reported anomalous hysteresis in the current–voltage curves by predicting the existence of photostable species under working conditions [56].

Although initial theoretical studies claimed the importance of relativistic effects for the heavy atoms in $MAPbX_3$ perovskites, the inclusion of such an effect was initially discussed by Even's group, who studied the effect of spin orbit coupling (SOC) on the electronic properties of these materials. In particular, comparing the effects of both DFT and DFT+SOC approaches on the low-T orthorhombic structure (P_{mma}) of $MAPbX_3$ (X = I, Br), Even's group observed giant spin orbit coupling associated with the conduction band [73]. Accordingly, for such polymorphs, the inclusion of SOC induces a lowering of the band gap by about 1 eV at the Γ point compared with the case of non-SOC DFT calculations (for $MAPbI_3$, $E_{gDFT} = 1.5$ eV, $E_{gDFT+SOC} = 0.5$ eV, and for $MAPbBr_3$, $E_{gDFT} = 1.9$ eV, $E_{gDFT+SOC} = 0.8$ eV). Such a lowering in energy shows the agreement between the DFT calculations and the experimental data (for $MAPbI_3$, $E_{g\ exp} = 1.5$ eV, and for $MAPbBr_3$, $E_{g\ exp} = 2.2$ eV [27]). However, this is simply the consequence of the large cancellation of errors, and thus is purely fortuitous. The shortcomings of the DFT method in predicting the band gaps of semiconductors do not allow us to calculate values in close agreement with the experimental values properly. Similarly, using a DFT+SOC approach, a comparison of perovskites containing different metals on the B site, i.e., $MAPbI_3$ and $MASnI_3$ [74], has been carried out. Here, the P_{4mm} structure (the α phase reported by Stoumpos [45]) was investigated. The hole effective mass was calculated for the two halide compounds and the DFT+SOC approach was found to give similar results to calculations of the same observable on the corresponding inorganic counterparts ($CsPbI_3$ and $CsSnI_3$) in the range 0.04–0.12 m_0. Recent studies combining dispersion interactions and relativistic effects have demonstrated the non-negligible impact of the former on the structural properties, while minor consequences are ascribed to the inclusion of SOC in the description of the lattice constants of these materials [77].

In this context, we performed DFT calculations [78, 79] focusing on both of the photocarrier effective masses in the conventional (pseudo) cubic phase of $MAPbI_3$ [80]. We have also shed light on the previously overlooked role that the organic cation plays in the electronic and optical properties of organic–inorganic perovskites. Even if it is well known that DFT-based methodologies do not properly describe the conduction and valence regions, DFT methods are able to confirm the experimentally reported ambipolarity of this class of materials [50–52]. Based on a parabolic approximation, we estimated the effective mass (m^*) of carriers at the bottom of the CB or the top of the VB as a result of a parabolic fit of the dispersion relationship. At the DFT level, the two carriers along the Γ–R–Γ direction have masses of $m_e^* = 0.32m_0$ and $m_h^* = 0.36m_0$, respectively. Further calculations using a large number of k points for sampling of the Brillouin zone show how these two values tend to overlap. The inclusion of relativistic effects quantitatively reduces the two carrier masses while still confirming the ambipolar nature of the materials. Once SOC effects are included, the new band gap was calculated to be 0.52 eV with $\Delta_o \sim 1.1$ eV [80].

A very interesting property related to organic–inorganic perovskites is the tendency of DFT to overestimate the mass of the lighter holes, in clear contrast with the fact that according to $k \cdot p$ theory for narrow-band-gap tetrahedral semiconductors, the same mass is underestimated as a consequence of the underestimation of the band gap itself [81]. Accurate values for the effective photocarrier masses were reported by Walsh's group [81]. In their paper, the quasi-self-consistent GW (QSGW) methodology, developed by van Schilfgaarde [82] and already successfully employed in the study of other semiconductors and electronic properties of alloys (see for example, Ref. [83]), was applied in an investigation into the electronic properties of both $MAPbI_3$ and NH_4PbI_3. Thus, using a combination of QSGW and SOC, in conjunction with a nonparabolic analytic expression to describe the Dresselhaus spin orbit coupling better, the k-dependent effective masses of both carriers in the dilute doping regime were calculated to be $m_h \sim 0.12m_0^*$ and $m_e \sim 0.15m_0^*$, respectively. These small values confirm the long diffusion length and the high mobility that characterize these materials, and once again confirm the ambipolar nature of $MAPbI_3$, even at the QSGW+SOC level of calculation. Figure 6 shows the band structure calculated at the QSGW level, including relativistic effects for both $CH_3NH_3PbI_3$ and NH_4PbI_3.
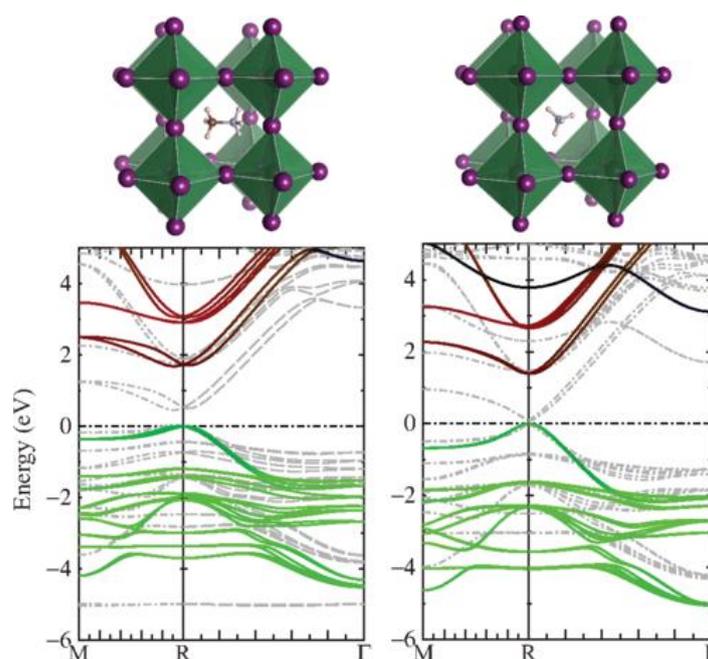
Fig. 6: *QS*GW band structure for $CH_3NH_3PbI_3$ (left-hand side) and NH_4PbI_3 (right-hand side). The light-gray dashed lines show the corresponding bands using the LDA approach. For full details, see Fig. 1 of Ref. [81]. (Reprinted figure with permission from Ref.[81]. Copyright (2014) by the American Physical Society.)

Using a method that included relativistic effects in an efficient GW approach [84, 85], Umari *et al.* [66] investigated the electronic properties of both MAPbI$_3$ and MASnI$_3$. The different relativistic effects of the masses of Pb and Sn are the key to understanding the distinct properties of these two perovskites as light harvesters in solar cells. In particular, MASnI$_3$ is a better electron transporter than MAPbI$_3$. Similarly, the enhanced tendency of the former compound to oxidize [45] was confirmed theoretically. Solving this issue is the key to the production of lead-free, environmentally friendly MASnI$_3$ devices, whose very promising performance has already been reported experimentally [86, 87].

Our group has recently provided clear evidence of the fundamental impact of the MA cation on the electronic properties of 3D MAPbI$_3$. Moving on from the work of Umebayashi *et al.* [88], who first investigated the electronic properties of low-dimensional crystals of mixed organic–inorganic halide perovskites, and attributed all the remarkable excitonic, optical, and electronic properties exclusively to the low-dimensional inorganic moieties (the $[PbI_6]^{-4}$ network), we extended a similar analysis to the 3D crystals [89]. In our study, we compared the structural and electronic properties of the cells shown in Fig. 7. Fig. 7(a) shows the cubic conventional fully

optimized cell (ions + lattice), Fig. 7(b) shows the fully optimized cell (ions + lattice) *without* an MA cation (bare semiconductor network), and Fig. 7(c) shows the result of removing the MA cation from the structure in Fig. 7(a), freezing the ionic positions and lattice parameters.
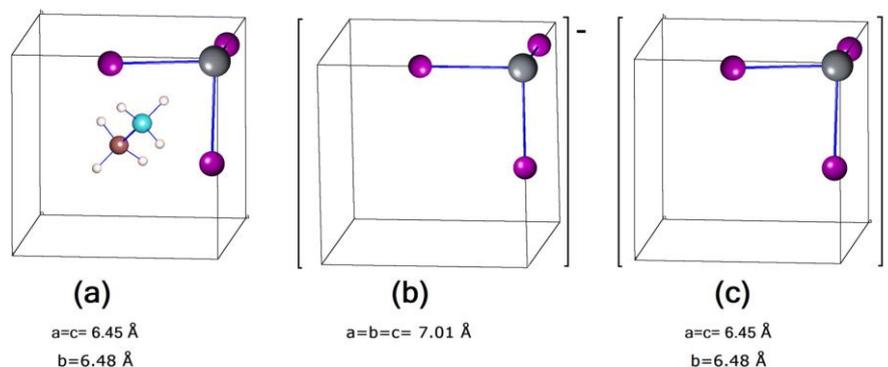

(a)

a=c= 6.45 Å
b=6.48 Å

(b)

a=b=c= 7.01 Å

(c)

a=c= 6.45 Å
b=6.48 Å

Fig. 7: (a) Optimized structure of the MAPbI$_3$ organic–inorganic halide perovskite. (b) Optimized structure of the [PbI$_3$]$^-$ inorganic network. (c) Single-point calculation of the geometry of the structure of Fig. 7(a) after the MA organic cation is removed. The lattice parameters and ionic positions of the inorganic network in Fig. 7(a) and Fig. 7 (c) are identical. Key large atoms: dark gray = lead, purple = iodine, brown = carbon. Key small atoms: light blue = nitrogen, white = hydrogen. (Reprinted with permission from Ref. [89]. Copyright (2014) American Chemical Society.)

The band gaps of the three systems are shown in Figs 8(a)–8(c), with Fig 8(d) showing the band structure calculated for the system in Fig. 8(a) at the DFT+SOC level of theory. The removal of the MA moiety and the subsequent structure optimization (Fig. 7(b)) leads to an expansion in cell volume from the disappearance of the NH···I long-range-bonding interactions. Such an increase in volume has the effect of reordering the band-edge population (Fig. 8(b)). The rise in energy of the I 5p orbitals that now form the new valence band maximum is ascribed to the fact that their overlap is only slightly affected by the increase in the size of the unit cell. The antibonding overlap between the localized Pb 6s and I 5p orbitals is decreased from the change in volume, with a subsequent energetic lowering of these bands inside the valence band.

Clearly, the presence of MA cations is responsible for the ambipolar nature of MAPbI$_3$. Its removal induces a flattening of the VBM, which confers a more marked electron transport character to the semiconductor network.
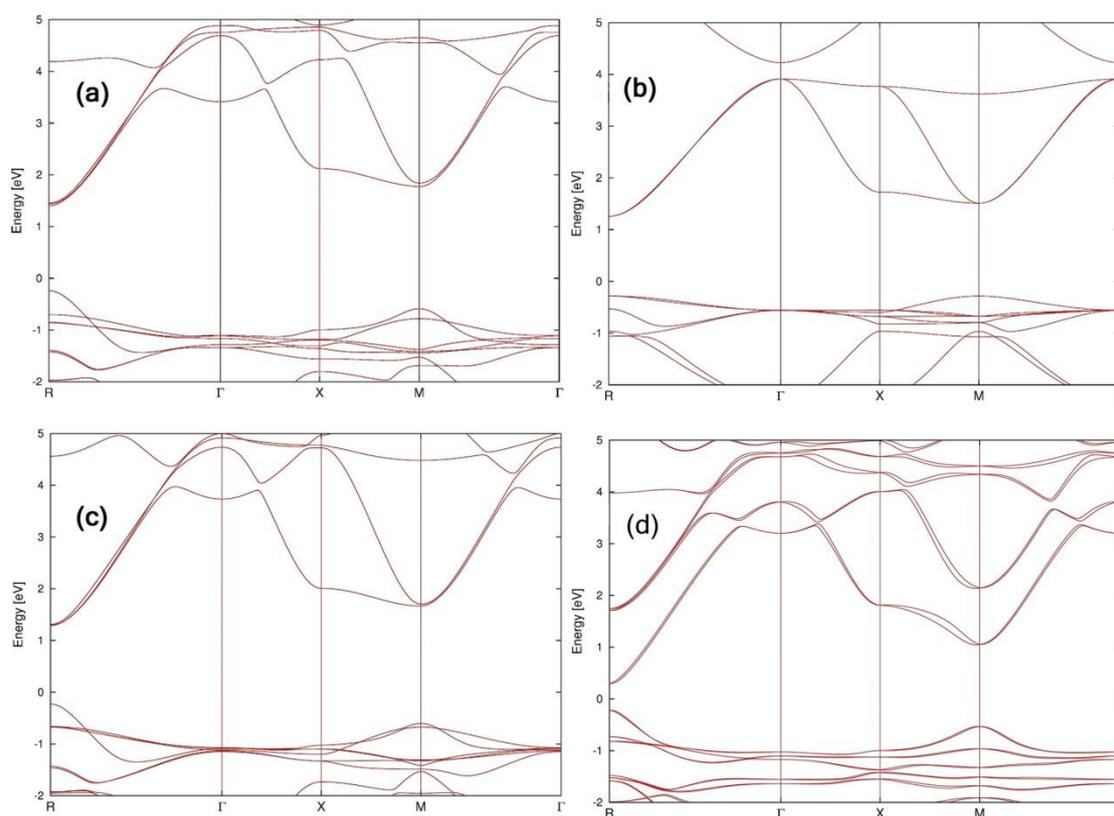
Fig. 8: Band structure of: (a) MAPbI$_3$ crystal ((*a*) structure); (b) the bare fully optimized [PbI$_3$]$^-$ network ((*b*) structure); and (c) the bare [PbI$_3$]$^-$ network ((*c*) structure). The same lattice parameters of the initially optimized MAPbI$_3$ ((*a*) structure) were used. (d) DFT+SOC-calculated band structure of the optimized (*a*) structure of MAPbI$_3$. The cubic symmetry points were used (R = 0.5, 0.5, 0.5; Γ = 0.0, 0.0, 0.0; M = 0.5, 0.5, 0.0; X = 0.5, 0.0, 0.0). (Reprinted with permission from Ref. [89]. Copyright 2014 American Chemical Society.)

From a comparison of the most studied fully inorganic halide perovskite, i.e., CsPbI$_3$, we noticed that whatever the nature of the A-site cation in the conventional cubic cell (i.e., Cs or MA), the CBM at the Γ point is always constituted by the A-site cation orbitals.

The band gap of the two perovskite compounds is not the same when calculated at the DFT, DFT+SOC, and DFT+SOC+HSE06 levels, being 1.48, 0.32, and 0.75 eV and 1.64, 0.52, and 0.96 eV for CsPbI$_3$ and MAPbI$_3$, respectively [89]. The reduction in the band gap of CsPbI$_3$ is mainly ascribed to its upward shift of the VBM. To check the origin of this behavior, we considered two deep, flat levels belonging to the PbI$_3$

network common to the two perovskites (from the $5d$ Pb and $5s$ I orbitals) and calculated the difference for both compounds. This simple procedure offers a valuable scheme for evaluating the band offset of the two perovskite systems.

A similar band offset value (5.12 vs. 5.14 eV) was observed. Thus, we aligned the VBM and CBM with respect to the deep (and flat) Pb $5d$ orbitals, finding, as stated, a slightly larger contribution because of the value of ΔE_{VBM} to the ΔE_G value between the two halides. Table 1 lists the ΔE value between the deep $5d$ Pb and $5s$ I orbitals, along with the band-edge energies at the R point for the MAPbI$_3$- and CsPbI$_3$-optimized structures. The band-edge energies are similarly reported for the CsPbI$_3$ structure using the lattice parameters of the optimized MAPbI$_3$ structure ($a = 6.45$ Å and $a = 6.48$ Å, respectively).

	MAPbI$_3$	CsPbI$_3$		CsPbI$_3$ a=6.45 Å		CsPbI$_3$ a=6.48 Å	
$\Delta E_{Pb/I}$	5.12	5.14		5.19		5.23	
E_{CBM}	-13.21	-12.68		-12.98		-13.20	
E_{VBM}	-14.85	-14.17		-14.52		-14.77	
ΔE_{CBM}			0.54		0.23		*0.01*
ΔE_{VBM}			0.68		0.33		*0.08*

Table 1: The difference in the $5d$ Pb and $5s$ I flat orbitals ($\Delta E_{Pb/I}$), and the band-edge energies at the R point for MAPbI$_3$- and CsPbI$_3$-optimized structures, and for the structure of CsPbI$_3$ where the lattice parameters of the optimized MAPbI$_3$ structure were imposed ($a = 6.45$ Å and $a = 6.48$ Å, respectively).

Thus, we applied the lattice parameters of MAPbI$_3$ to CsPbI$_3$ and similarly calculated the band structure and aligned the band edges, and found that increasing the lattice parameters of CsPbI$_3$ led to a sensitive approach towards the MAPbI$_3$ band-edge energy. For $a = 6.48$ Å, the value of E_{CBM} for CsPbI$_3$ almost coincided with that for MAPbI$_3$ (i.e., it was slightly larger, but almost negligible for ΔE_{VBM}, see Table 1). This finding can be explained by the fact that the VBM of both perovskites consists of a combination of the Pb $6s$ and I $5p$ antibonding orbitals, with both orbitals being major contributors. In the case of CsPbI$_3$, whose optimized lattice parameters are

reduced ($a = 6.41$ for $CsPbI_3$ vs. $a = c = 6.45$ and $b = 6.48$ Å for $MAPbI_3$), a higher degree of overlap will lead to an increase in the VBM energy. Thus, the decrease in band gap stems directly from the reduction in unit cell volume in the case of $CsPbI_3$ (increase in E_{VBM}). The fact that the band gap is controlled by the Pb s - I p antibonding interactions is in clear agreement with previous results reported for $CsSnX_3$ (X = Cl, Br, I) [90].

3. Conclusions

We have provided an overview of the state of the art concerning the ongoing experimental and theoretical investigations into the properties of the class of organic–inorganic halide perovskites. We have shown that there is plenty of room for further improvement in the properties of these mixed organic–inorganic halide perovskites, as testified by the impressive achievements obtained in less than six years since their first use in PV systems (i.e., since 2009 [46]). Similarly, we have shown how the synergistic interaction between experimentalists and theoreticians is the key to elucidating the potential of these materials in solar devices. Realistically, certified PCEs approaching 20% may be achieved in a very short time [91] (in addition, there is the possibility of utilizing more environmentally friendly Pb-free devices), opening the way to the commercial mass production of solar cells based on the use of this versatile class of materials.

Bibliography

[1] V. M. Goldschmidt, *Die Naturwissenschaften,*1926, **21**, 477–485.

[2] A. M. Glazer, *Acta Cryst.,*1972, **B28**, 3384-3392.

[3] M. Johnsson, P. Lemmens, Crystallography and Chemistry of Perovskites, Handbook of Magnetism and Advanced Magnetic Materials, H. Kronmueller, S. Parkin (Eds.), John Wiley & Sons, Ltd., New York (2006).

[4] A.F. Wells, *Structural Inorganic Chemsitry*, Oxford Science publications, London, (1995).

[5] U. Müller, *Inorganic Structural Chemistry*, Wiley & Sons Ltd, Chichester (1993).

[6] A. S. Bhalla, R. Guo, R. Roy, *Mater. Res. Innovat*., 2000, **4**, 3-26.

[7] J.-H. Sohn, Y. Inaguma, S.-O. Yoon, M. Itoh, T. Nakamura, S.-J. Yoon, H.-J. Kim, *Jpn. J. Appl. Phys*., 1994, **33** 5466-5470.

[8] X.- C. Liu, R. Hong, C. Tian, *J. Mater. Sci.: Mater. Electron.* 2009, **20**, 323-327.

[9] A. M. Glazer, *Acta Cryst.,*1975, **A31**, 756-762.

[10] B. Jaffe, W. R. Cook Jr., H. Jaffe, *Piezoelectric Ceramics*, J. P. Roberts & P. Popper Editors, Academic Press, London (1971).

[11] R. Whatmore, *Rep. Prog. Phys.*, 1986, **49**, 1335-1386.

[12] Physics of Manganites, T.A. Kaplan and S.D. Mahanti Editors, Kluwer/Plenum, New York (1999).

[13] Y. Maeno, H. Hashimoto, K. Yoshida, S. Nishizaki, T. Fujita, J. G. Bednorz and F. Lichtenberg, *Nature,* 1994, **372**, 532-534.

[14] G. Yi, Z. Wu and M. Sayer, *J. Appl. Phys.*, 1988, **64**, 2717-2724.

[15] M. Yang, J. Oró-Solé, J. A. Rodgers, A. B. Jorge, A. Fuertes and J. P. Attfield, *Nat. Chem.*, 2011, **3**, 47–52.

[16] D. B. Mitzi, *Inorg. Chem.*, 2000, **39**, 6107– 6113.

[17] D. B. Mitzi, C. A. Feild, W.T.A. Harrison and A.M. Guloy, *Nature,*1994, **369**, 467– 469.

[18] C.R. Kagan, D.B. Mitzi and C.D. Dimitrakopoulos, *Science,*1999, **286**, 945– 947.

[19] J. Calabrese , N. L. Jones , R. L. Harlow , N. Herron , D. L. Thorn and Y. Wang, *J. Am. Chem. Soc.*, 1991, **113**, 2328–2330.

[20] K. Liang, D. B. Mitzi and M. T. Prikas, *Chem. Mater.*, 1998, **10**, 403-411.

[21] D. B. Mitzi, S. Wang, C. A. Feild, C. A. Chess and A. M. Guloy, *Science*, 1995, **267**, 1473-1476.

[22] G. Kieslich, S. Sun and A. K. Cheetham, *Chem. Sci.*, 2014, DOI: 10.1039/c4sc02211d

[23] D. B. Mitzi, *J. Chem. Soc., Dalton Trans.*, 2001, 1–12.

[24] J. Burschka, N. Pellet, S.-J. Moon, R. Humphry-Baker, P. Gao, M. K. Nazeeruddin and M. Grätzel, *Nature*, 2013, **499**, 316–319.

[25] M. Liu, M. B. Johnston and H. J. Snaith, *Nature*, 2013, **501**, 395-398.

[26] K. Wojciechowski, M. Saliba, T. Leijtens, A. Abate and H. J. Snaith, *Energy Environ. Sci.*, 2014, **7**, 1142-1147.

[27] J. H. Noh, S. H. Im, J. H. Heo, T. N. Mandal and S. I. Seok, *Nano Lett.,* 2013, **13**, 1764– 1769.

[28] J. H. Heo, S. H. Im, J. H. Noh, T. N. Mandal, C. S. Lim, J. A. Chang, Y. H. Lee, H. J. Kim, A. Sarkar, M. K. Nazeeruddin, M. Grätzel and S. I. Seok, *Nat. Photonics*, 2013, **7**, 487– 492.

[29] H.-S. Kim, C.R. Lee, J.H. Im, K.B. Lee, T. Moehl, A. Marchioro, S.J. Moon, R. Humphry-Baker, J. H. Yum, J. E. Moser, M. Grätzel and N.G. Park, *Sci. Rep.*, 2012, **2**, 591– 7.

[30] S. Kazim, M. K. Nazeeruddin, M. Gräztel and S. Ahmad, *Angew. Chem. Int. Ed.*, 2014, **53**, 2-15.

[31] P. Gao, M. Grätzel and M. K. Nazeruddin, *Energy Environ. Sci.*, 2014,**7**, 2448-2463.

[32] H.-S. Kim, S. H. Im and N.-G. Park, *J. Phys. Chem. C*, 2014, **118**, 5615–5625.

[33] T. C. Sum and N. Mathews, *Energy Environ. Sci.*, 2014, **7**, 2518-2534.

[34] S. A. Bretschneider, J. Weickert, J. A. Dorman and L. Schmidt-Mende, *APL Mat.*, 2014, **2**, 040701-9.

[35] P. V. Kamat, *J. Am. Chem. Soc.*, 2014, **136**, 3713–3714.

[36] M. Grätzel, *Nat. Materials*, 2014, **13**, 838-842.

[37] M. A. Green, A. Ho-Baillie and H. J. Snaith, *Nat. Photonics*, 2014, **8**, 506-514.

[38] N. G. Park, Materials Today, DOI: 10.1016/j.mattod.2014.07.007

[39] A. Poglitsch and D. Weber, *J. Chem. Phys.*,1987, **87**, 6373– 6378.

[40] G. C. Papavassiliou, *Prog. Solid State Chem.*, 1997, **25**, 125–270.

[41] Y. Takahashi, R. Obara, Z. Lin, Y. Takahashi, T. Naito, T. Inabe, S. Ishibashi and K. Terakura, *Dalton Trans.*, 2011, **40**, 5563– 5568.

[42] K. Yamada, K. Nakada, Y. Takeuchi, K. Nawa and Y. Yamane, *Bull. Chem. Soc. Jpn.*, 2011, **84**, 926– 932.

[43] D. Weber, *Z. Naturforsch., B: Anorg. Chem., Org. Chem.*, 1978, **33**, 1443-1445.

[44] Y. Kawamura, H. Mashiyama and K. Hasebe, *J. Phys. Soc. Jpn.*, 2002, **71**, 1694–1697.

[45] C.C. Stoumpos, C. D. Malliakas and M.G. Kanatzidis, *Inorg. Chem.*, 2013, **52**, 9019– 9038.

[46] A. Kojima, K. Teshima, Y. Shirai and T. Miyasaka, *J. Am. Chem. Soc.*, 2009, **131**, 6050– 6051.

[47] J.-H. Im, C.-R Lee, J.-W. Lee, S.-W. Park and N.-G. Park, *Nanoscale*, 2011, **3**, 4088-4093.

[48] D. Bi, L. Yang, G. Boschloo, A. Hagfeldt and E. M. J. Johansson, *J. Phys. Chem. Lett.*, 2013, **4**, 1532−1536.

[49] J. H. Noh, N. J. Jeon, Y. C. Choi, *J. Mater. Chem. A*, 2013, **1**, 11842-11847.

[50] L. Etgar, P. Gao, Z. Xue, Q. Peng, A. K. Chandiran, B. Liu, M. K. Nazeeruddin and M. Grätzel, *J. Am. Chem. Soc.,* 2012, **134**, 17396– 17399.

[51] W.A. Laban and L. Etgar, *Energy Environ. Sci.*, 2013, **6**, 3249-3253.

[52] M. M. Lee, J. Teuscher, T. Miyasaka, T. N. Murakami and H. J. Snaith, *Science,* 2012, **338**, 643-647.

[53] G. Xing, N. Mathews, S. Sun, S. S. Lim, Y. M. Lam, M. Grätzel, S. Mhaisalkar and T. C. Sum, *Science,* 2013, **342**, 344-347.

[54] S. D. Stranks, G. E. Eperon, G. Grancini, C. Menelaou, M. J. P. Alcocer, T. Leijtens, L. M. Herz, A. Petrozza and H. J. Snaith, *Science*, 2013, **342**, 341-344.

[55] J. M. Ball, Michael M. Lee, A. Hey and H. J. Snaith, *Energy Environ. Sci.*, 2013, **6**, 1739-1743.

[56] H. J. Snaith, A. Abate, J. M. Ball, G. E. Eperon , T. Leijtens , N. K. Noel, S. D. Stranks , J. T.-W. Wang, K. Wojciechowski and W. Zhang, *J. Phys. Chem. Lett.*, 2014, **5**, 1511–1515.

[57] Q. Chen, H. Zhou, Z. Hong, S. Luo, H.-S. Duan, H.-H. Wang, Y. Liu, G. Li and Y. Yang, *J. Am. Chem. Soc.*, 2014, **136**, 622– 625.

[58] J. Kim, S.-H. Lee, J. H. Lee and K.-H. Hong, *J. Phys. Chem. Lett.*, 2014, **5**, 1312–1317.

[59] W.-J. Yin, T. Shi and Y. Yan, *Appl. Phys. Lett.*, 2014, **104**, 063903-4.

[60] M. H. Du, *J. Mater. Chem. A*, 2014, **2**, 9091-9098.

[61] J. Haruyama, K. Sodeyama, L. Han and Y. Tateyama, *J. Phys. Chem. Lett.*, 2014, **5**, 2903–2909.

[62] E. Mosconi, A. Amat, Md. K. Nazeeruddin, M. Grätzel, and F. De Angelis, *J. Phys. Chem. C*, 2013, **117**, 13902–13913.

[63] S. Colella, E. Mosconi, P. Fedeli, A. Listorti, F. Gazza, F. Orlandi, P. Ferro, T. Besagni, A. Rizzo, G. Calestani, G. Gigli, F. De Angelis and R. Mosca, *Chem. Mater.*, 2013, **25**, 4613-4618.

[64] V. Roiati, E. Mosconi, A. Listorti, S. Colella, G. Gigli and F. De Angelis, *Nano Lett.*, 2014, **14**, 2168-2174.

[65] C. Quarti, G. Grancini, E. Mosconi, P. Bruno, J. M. Ball, M. M. Lee, H. J. Snaith, A. Petrozza and F. De Angelis, *J. Phys. Chem. Lett.*, 2014, **5**, 279–284.

[66] P. Umari, E. Mosconi and F. De Angelis, *Sci. Rep.*, 2014, **4**, 4467.

[67] F. De Angelis, *Acc. Chem. Res.*, 2014, Article ASAP, DOI: 10.1021/ar500089n.

[68] A. Amat, E. Mosconi, E. Ronca, C. Quarti, P. Umari, Md. K. Nazeeruddin, M. Grätzel and F. De Angelis, *Nano Lett.*, 2014, **14**, 3608-3616.

[69] R. Gottesman, E. Haltzi, L. Gouda, S. Tirosh, Yaniv Bouhadana, A. Zaban, E. Mosconi and F. De Angelis, *J. Phys. Chem. Lett.*, 2014, **5**, 2662–2669.

[70] J. Even, L. Pedesseau and C. Katan, *J. Phys. Chem. C*, 2014, **118**, 11566–11572.

[71] J. Even, L. Pedesseau, J.-M. Jancu and C. Katan, *J. Phys. Chem. Lett.*, 2013, **4**, 2999– 3005.

[72] J. Even, L. Pedesseau, J.-M. Jancu and C. Katan, *Phys. Status Solidi Rapid Res. Lett.*, 2014, **8**, 31–35.

[73] J. Even, L. Pedesseau and C. Katan, *ChemPhysChem*, DOI: 10.1002/cphc.201402428.

[74] J. Even, L. Pedesseau, E. Tea, S. Almosni, A. Rolland, C. Robert, J.-M. Jancu, C. Cornet, C. Katan, J.-F. Guillemoles and O. Durand, *International Journal of Photoenergy*, 2014, **2014**, 649408.

[75] C. Wehernfennig, G. E. Eperon, M. B. Johnston, H. J. Snaith and L. M. Herz, *Adv. Mater.*, 2014, **26**, 1584-1589.

[76] J. M. Frost, K. T. Butler, F. Brivio, C. H. Hendon, M. van Schilfgaarde and A. Walsh, *Nano Lett.*, 2014, **14**, 2584– 2590.

[77] D. A. Egger and L. Kroonik, *J. Phys. Chem. Lett.*, 2014, **5**, 2728– 2733.

[78] G. Kresse and J. Furthmüller, *Comput. Mater. Sci.*, 1996, **6**, 15-50.

[79] G. Kresse and J. Furthmüller, *Phys. Rev. B*, 1996, **54**, 11169-11186.

[80] G. Giorgi, J.-I. Fujisawa, H. Segawa and K. Yamashita, *J. Phys. Chem. Lett.*, 2013, **4**, 4213– 4216.

[81] F. Brivio, K. T. Butler, A. Walsh and M. van Schilfgaarde, *Phys. Rev. B*, 2014, **89**, 155204-6.

[82] M. van Schilfgaarde, T. Kotani and S. Faleev, *Phys. Rev. Lett.*, 2006, **96**, 226402-4.

[83] G. Giorgi, M. Van Schilfgaarde, A. Korkin and K. Yamashita, *Nanoscale Res. Lett.,* 2010, **5**, 469-477.

[84] P. Umari, J. Stenuit and S. Baroni, *Phys. Rev. B*, 2009, **79**, 210104-4(R).

[85] P. Umari, J. Stenuit and S. Baroni, *Phys. Rev. B*, 2010, **81**, 115104-5.

[86] N. K. Noel, S. D. Stranks, A. Abate, C. Wehrenfennig, S. Guarnera, A. Haghighirad, A. Sadhanala, G. E Eperon, S. K. Pathak, M. B Johnston, A. Petrozza, L. Herz and H. Snaith, *Energy Environ. Sci.*, 2014, **7**, 3061-3068.

[87] F. Hao, C. C. Stoumpos, D. H. Cao, R. P. H. Chang and M. G. Kanatzidis, *Nat. Photonics*, 2014, **8**, 489–494.

[88] T. Umebayashi, K. Asai, T. Kondo and A. Nakao, *Phys. Rev. B*, 2003, **67**, 155405-6.

[89] G. Giorgi, J.-I. Fujisawa, H. Segawa and K. Yamashita, *J. Phys. Chem. C*, 2014, **118**, 12176–12183.

[90] L.-y. Huang, W. R. L. Lambrecht, *Phys. Rev. B*, 2013 **88**, 165203-12.

[91] N.-G. Park, *J. Phys. Chem. Lett.*, 2013, **4**,
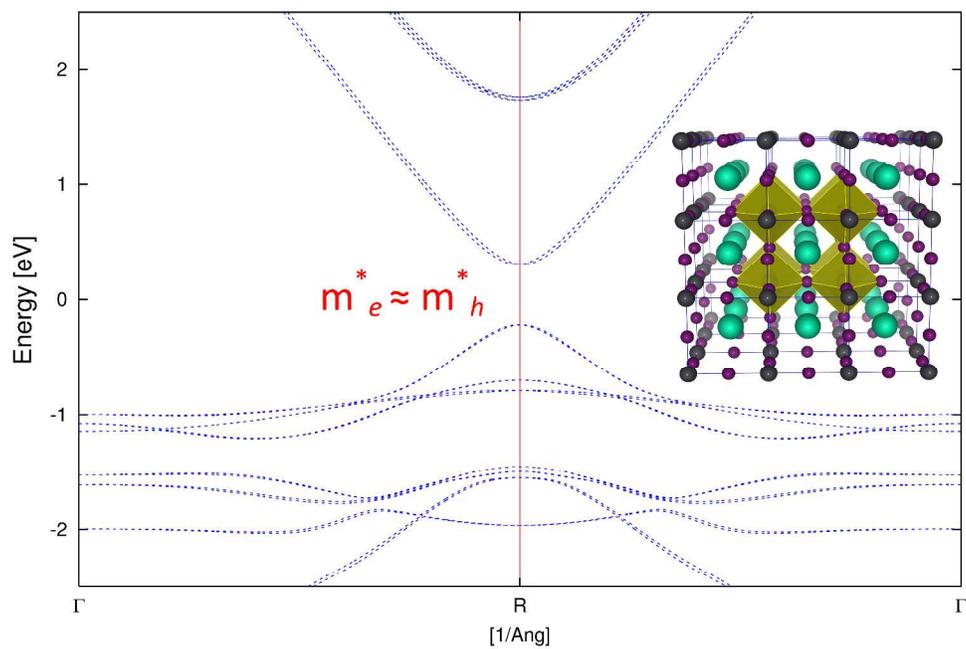
The synergistic interaction between experimentalists and theoreticians discloses the potentialities of hybrid organic-inorganic halide perovskites in their application in PV.